

Demonstration of Maxwell Demon-assistant Einstein-Podolsky-Rosen Steering via Superconducting Quantum Processor

Z. T. Wang,^{1,*} Ruixia Wang,^{1,*} Peng Zhao,¹ Z. H. Yang,^{2,3}
 Kaixuan Huang,¹ Kai Xu,^{2,1,4} Yong-Sheng Zhang,^{5,6,7,†} Heng
 Fan,^{2,1,3,4,7,8} S. P. Zhao,^{2,3,4,8} Meng-Jun Hu,^{1,‡} and Haifeng Yu^{1,7}

¹*Beijing Academy of Quantum Information Sciences, Beijing 100193, China*

²*Beijing National Laboratory for Condensed Matter Physics,
 Institute of Physics, Chinese Academy of Sciences, Beijing 100190, China*

³*School of Physical Sciences, University of Chinese Academy of Sciences, Beijing 100190, China*

⁴*CAS Center for Excellence in Topological Quantum Computation, UCAS, Beijing 100190, China*

⁵*Laboratory of Quantum Information, University of Science and Technology of China, Hefei 230026, China*

⁶*Synergetic Innovation Center of Quantum Information and Quantum Physics,
 University of Science and Technology of China, Hefei 230026, China*

⁷*Hefei National Laboratory, University of Science and Technology of China, Hefei, 230088, China*

⁸*Songshan Lake Materials Laboratory, Dongguan 523808, China*

(Dated: November 21, 2023)

The concept of Maxwell demon plays an essential role in connecting thermodynamics and information theory, while entanglement and non-locality are fundamental features of quantum theory. Given the rapid advancements in the field of quantum information science, there is a growing interest and significance in investigating the connection between Maxwell demon and quantum correlation. The majority of research endeavors thus far have been directed towards the extraction of work from quantum correlation through the utilization of Maxwell demon. Recently, a novel concept called Maxwell demon-assistant Einstein-Podolsky-Rosen (EPR) steering has been proposed, which suggests that it is possible to simulate quantum correlation by doing work. This seemingly counterintuitive conclusion is attributed to the fact that Alice and Bob need classical communication during EPR steering task, a requirement that does not apply in the Bell test. In this study, we demonstrate Maxwell demon-assistant EPR steering with superconducting quantum circuits. By compiling and optimizing a quantum circuit to be implemented on a 2D superconducting chip, we

were able to achieve a steering parameter of $S_2 = 0.770 \pm 0.005$ in the case of two measurement settings, which surpasses the classical bound of $1/\sqrt{2}$ by 12.6 standard deviations. In addition, experimental observations have revealed a linear correlation between the non-locality demonstrated in EPR steering and the work done by the demon. Considering the errors in practical operation, the experimental results are highly consistent with theoretical predictions. Our findings not only suggest the presence of a Maxwell demon loophole in the EPR steering, but also contribute to a deeper comprehension of the interplay between quantum correlation, information theory, and thermodynamics.

* These authors contribute equally

† yshzhang@ustc.edu.cn

‡ humj@baqis.ac.cn

Introduction. Non-locality is a key characteristic of quantum theory, which sets it apart from traditional theories that adhere to local realism [1–3]. In his pioneering paper, Bell shows that quantum theory refutes any local hidden variable models [4]. Since then, great efforts have been made to verify this Bell non-locality with loopholes closed using the Bell-CHSH inequality [5–16]. Non-locality is attributed to quantum correlation, and the existence of its hierarchy has been shown, especially when Einstein-Podolsky-Rosen (EPR) steering was discovered by Wiseman *et al* [17]. EPR steering, which refutes any local hidden state models, is a form of non-locality that lies between Bell non-locality and non-separability [18].

From an information theory standpoint, it can be observed that the entropy of an entangled quantum system is comparatively lower than that of mixed systems after measurements. The observation suggests that the entangled system contains additional information that can be harnessed to generate useful work [19]. Since the concept of the Maxwell demon is deeply connected to both thermodynamics and information [20], it is natural to consider the interplay between the Maxwell demon and quantum correlations. Zurek initially conducted an analysis of Szilard’s one-molecule engine in the quantum domain [21]. Subsequently, he provided evidence to support the notion that the efficiency disparity between quantum and classical Maxwell demons, in terms of extracting work from correlated quantum systems [22], is determined by quantum discord, a metric for quantifying quantum correlations. Numerous studies then have been conducted on the detection of entanglement through the utilization of Maxwell’s demon [23–27]. In recent years, there has been a significant surge of interest in the quantum heat engine (QHE) [28–32] that incorporates the Maxwell demon, primarily driven by the rapid advancements in quantum information science and technology. Whether quantum resources, such as quantum correlation, can demonstrate the quantum advantage of QHE has been a central topic of investigation [33–35].

To date, researchers have primarily focused their attention on extracting work by leveraging quantum correlation [36–38]. It is both intriguing and significant to contemplate alternative viewpoints and inquire about the possibility of simulating quantum correlation or non-locality through the application of work. In a recent study, the authors (including two of the present authors) provide a positive response to the question posed [39]. The incorporation of a Maxwell demon into the EPR steering task has been demonstrated, enabling collaboration between Alice and the demon to deceive Bob through the use of local operations and classical communication. The reason for this discrepancy lies in the presence of information exchange between Alice and Bob during the task of EPR steering, a phenomenon that is not possible in the context of the Bell test. The concept of

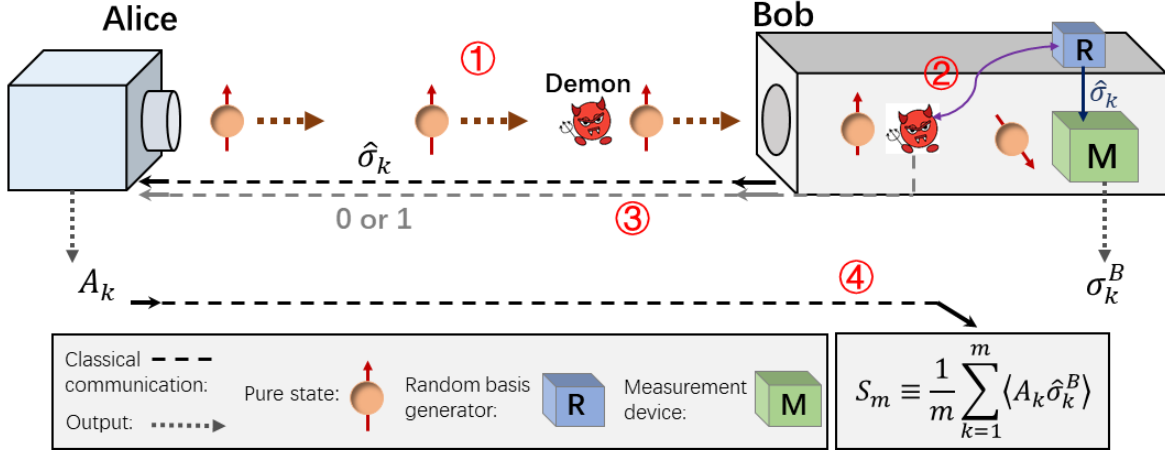


FIG. 1. The Maxwell Demon-assisted EPR steering task. **(1)**: Bob receives qubits sent by Alice, meanwhile the demon sneaks into Bob’s device along with qubits. All qubits are prepared in the same pure state. **(2)**: The demon gains access to the information of the measurement setting $\hat{\sigma}_k$ by entangling itself with Bob’s random basis generator. The demon then randomly rotates the qubits into one of the eigenstates of $\hat{\sigma}_k$ before Bob performs measurements. **(3)**: Bob announces his measurement setting $\hat{\sigma}_k$ to Alice, meanwhile the demon secretly sends an additional 1 bit of information to Alice, which is mixed in the communication channel between Bob and Alice. The 1 bit information tells Alice which eigenstate of $\hat{\sigma}_k$ it has chosen to rotate the qubits into. **(4)**: Based on the information provided by Bob and the demon, Alice responds to Bob regarding her result A_k . **(1)-(4)** are repeated multiple times, and Bob combines the results to calculate the steering parameter S_m . If S_m exceeds a certain classical bound, then Bob becomes convinced that Alice has the ability to remotely manipulate his state. It should be noted that the demon may not do operations for every run, and in this case, Alice answers Bob randomly.

the Maxwell demon-assisted EPR steering introduces a new loophole in thermodynamics, which is distinct from existing loopholes related to locality, free will, and detection. The closure of this demon loophole requires continuous monitoring of Bob’s surroundings to ensure that there are no abnormal heat fluctuations caused by the demon’s attempts to erase its memory. In order to investigate the correlation between the work performed by the demon and the non-locality exhibited in the EPR steering, a dedicated quantum circuit model has been proposed [39]

In this work, we experimentally demonstrate the Maxwell demon-assisted EPR steering with superconducting qubits as the demon [40]. The measurement and feedback of the demon are implemented via appropriate gate operations. The process of erasing a demon’s memory involves

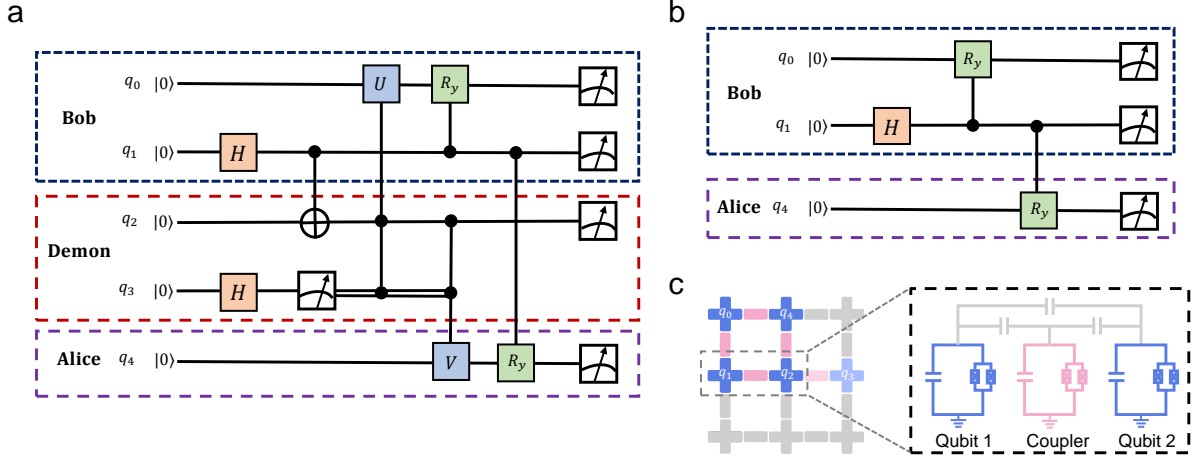


FIG. 2. **a:** Quantum circuit representation of Maxwell demon-assisted EPR steering with two measurement settings $\{\hat{\sigma}_Z, \hat{\sigma}_X\}$. **b:** Quantum circuit representation without the Maxwell demon. **c:** Schematic diagram of a superconducting quantum processor in which the physical qubits $q_0 - q_4$ correspond to the logical qubits $q_0 - q_4$ in the quantum circuit. In the practical experiment, we execute circuit **a** or circuit **b** with a certain probability p to simulate the case that the demon performs operations probabilistically.

resetting qubits to their ground state, which results in the emission of microwave photons into the local environment. By compiling and optimizing a demon circuit to accommodate the physical qubits on a 9-qubit superconducting chip, we have observed quantum correlation between Alice and Bob, where the EPR steering parameter exceeds the classical bound. More significantly, we have successfully validated the linear correlation between the non-locality exhibited in EPR steering and the work performed by the demon.

Maxwell demon-assisted EPR steering. The illustration of Maxwell demon-assisted EPR steering is presented in Fig. 1. The qubits, accompanied by the demon, are sent to Bob by Alice. All qubits are initialized in the identical state $|0\rangle$. After infiltrating Bob's device, the demon will entangle itself with the random basis generator utilized by Bob to determine the measurement settings. Suppose that the standard state of the demon is denoted as $|D = 0\rangle$. The entangled state can be expressed as $\sum_{k=1}^m |D = k\rangle \otimes |k\rangle$, where the orthogonal states $\{|k\rangle\}$ of the generator represent Bob's different measurement settings choices $\{\hat{\sigma}_k\}$. After selecting one of the measurement settings $\hat{\sigma}_k$, and before the qubit measurement, there exists a temporal window during which the demon has the ability to manipulate the qubit through various operations. The demon randomly induces the rotation of the qubit into one of the eigenstates of the operator $\hat{\sigma}_k$. When establishing a classical

communication channel with Alice, Bob includes the transmission of his measurement setting. Additionally, the demon provides Alice with one bit of information regarding the eigenstates to which the qubit has been rotated. Based on the information provided by Bob and Demon, Alice responds to Bob by providing her result, denoted as A_k , in order to ensure a positive or anti-correlation with Bob's result. The presence of the aforementioned protocol can be attributed to the necessity for Bob and Alice to engage in classical communication during the EPR steering, a requirement that does not apply in the Bell test.

Currently, the majority of non-locality tests are conducted using photonic systems. However, it appears to be challenging to demonstrate Maxwell demon-assistant EPR steering, as depicted in Fig. 1. Fortunately, the corresponding quantum circuit model provides a promising way to demonstrate it on current quantum processors [41]. The Fig. 2a illustrates a specific quantum circuit representation of Maxwell demon-assistant EPR steering with two measurement settings $\{\hat{\sigma}_Z, \hat{\sigma}_X\}$. The demon is composed of two qubits, in which one qubit q_2 is entangled with Bob's basis generator q_1 via *CNOT* gate, and the another q_3 is used to determine the rotation of qubit q_0 to be measured. The crucial component of the circuit is the three qubits control-control- U gate, which describes the demon do operation on the qubit based on the obtained measurement setting information. Specifically, the operation U is determined as [39]

$$U|b\rangle_{q_3}|a\rangle_{q_2}|0\rangle_{q_0} = |b\rangle_{q_3}|a\rangle_{q_2} \otimes e^{-i\frac{\pi}{4}(a+2b)\hat{\sigma}_Y}|0\rangle_{q_0} \quad (1)$$

with $a, b \in \{0, 1\}$. In the given context, the variable a is used to represent different measurement settings. Specifically, when $a = 0$, it corresponds to the measurement setting $\hat{\sigma}_Z$, while $a = 1$ represents the measurement setting $\hat{\sigma}_X$. On the other hand, the variable b takes the values of either 0 or 1 corresponding to +1 or -1 eigenstate of chosen setting, respectively. For instance, when $a = 1$ and $b = 0$, it follows that the measurement setting $\hat{\sigma}_X$ is selected, and the qubit q_0 is rotated into its +1 eigenstate $|+\rangle = (|0\rangle + |1\rangle)/\sqrt{2}$. The circuit incorporates the control-control- V gate and the control- R_y gate, which together simulate the process of Alice responding to Bob using information obtained from the demon and Bob. The operators V and U are subject to the condition $\langle 0|V^\dagger U|0\rangle = 1$ in order to replicate a positive correlation in our experiment. In each run, the demon has to erase its memory to the standard state $|D = 0\rangle$, which is equivalent to resetting the qubits in the circuit. The process of memory erasure, as described by Landauer's erasure principle [42], results in the dissipation of energy into the local environment. Specifically, this energy is emitted as microwave photons within the circuit case. In order to mitigate the likelihood of detection

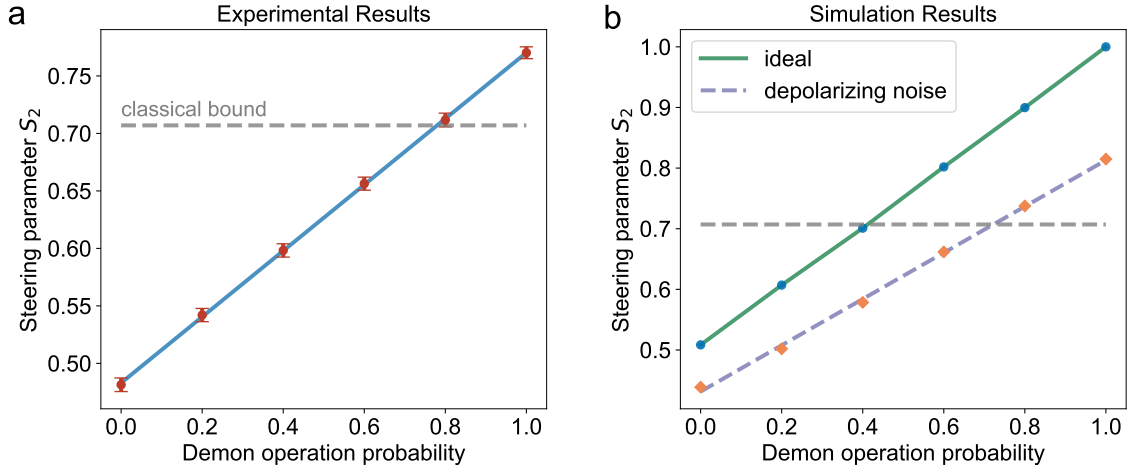


FIG. 3. **a**: Experimental results verify the linear relationship between the probability of demon operation p and the steering parameter S_2 , as predicted by theory. The largest value of S_2 is measured to be 0.770 ± 0.005 , which exceeds the classical bound of $1/\sqrt{2}$ by 12.6 standard deviations. **b**: Simulation results show that the deviation between the experiment and the ideal case is primarily caused by depolarizing noise in the actual circuits.

by Bob, the demon should perform operations probabilistically during each run. For the scenario where the demon remains inactive, Alice responds to Bob in a random manner. The corresponding quantum circuit is illustrated in Fig. 2b. Suppose that the demon do operations with a probability of p for each run. The resulting steering parameter S_2 is determined by [39].

$$S_2 = \frac{1}{2}(1 + p). \quad (2)$$

When $p > \sqrt{2} - 1$, EPR steering is demonstrated. Given that the reset process of qubits remains consistent across multiple experimental runs, the equation presented above illustrates the linear correlation between the non-locality demonstrated in EPR steering and the work performed by the demon.

Experimental results. The experiment is performed on a transmon-type two-dimensional square grid superconducting processor, as depicted in Figure 2c. The processor consists of 9 qubits and 12 couplers, with five qubits $q_0 - q_4$ being utilized for executing the quantum circuits. The fabrication of the superconducting chip involves the utilization of flip-chip technology, incorporating a tantalum base layer [43]. Each qubit in the device is in Xmon form and controlled by the control line combining microwave drive (XY control) and flux bias (Z control). The quantum state of each qubit is achieved through capacitive coupling to a quarter-wave resonator, enabling the simultane-

ous achievement of states for all qubits. The nearest neighbor qubits are connected by the coupler which is also a transmon qubit. The effective coupling strength of neighboring qubits can be continuously adjusted from $\sim +2\text{MHz}$ to $\sim -50\text{MHz}$ by manipulating the frequency of the coupler using an individual flux bias line. The energy relaxation time T_1 for each qubit at the idle point is around $30\ \mu\text{s}$, and the dephasing time T_2^* varies from $1.60\ \mu\text{s}$ to $4.23\ \mu\text{s}$. One triggering period lasts for $310\ \mu\text{s}$, and the remaining duration after the operation allows ample time for the qubits to reset to the state $|0\rangle$. In our experiment, all single qubit gates are implemented by using cosine enveloped pulses, and we employ the derivative removal by adiabatic gate (DRAG) technique to effectively minimize leakage [44]. The non-adiabatic CZ gate is implemented by adjusting the energy levels gradually with an error function-shaped pulse. We optimize the square pulses of the qubits and the couplers in order to mitigate leakage and attain the intended conditional phases of the CZ gate. By using Randomized Benchmarking (RB) [45], we are able to attain an average fidelity of 99.9% for single qubit gate and 99% for the two-qubit CZ gate, respectively (see Appendix A-D for more details).

With high-fidelity single-qubit gates and two-qubit CZ gates as the elementary gates, the quantum circuit of Maxwell demon-assistant EPR steering can be decomposed into the sequence of elementary gates. In order to ensure accurate results, we map the logical qubits onto the physical qubits of the quantum device in such a way that the depth of the executed quantum circuits is as shallow as possible. The most important operation in the circuit is the three qubits control-control- U gate described by Eq. (1). Since the quantum operation between q_0 and q_2 depends on the measurement results of q_3 , which acts as a random choice generator for the demon, we can divide the original circuit into two equivalent sub-circuits. Each sub-circuit consists of only two qubit operations, based on the two possible results of q_3 . The two sub-circuits can be further compiled and optimized into elementary gates based on the structure of the quantum device (see Appendix E for more details). In the Maxwell demon-assistant EPR steering experiment, we first perform a measurement on q_3 and then execute the corresponding sub-circuit based on its measurement result.

In this experiment, we execute the quantum circuit of Maxwell demon-assistant EPR steering with probability p varying from 0 to 1 to simulate the case that the demon performs operations probabilistically. The experimental results are given in Fig. 3a, illustrating a distinct linear correlation between the steering parameter S_2 and the operational probability of the Maxwell demon. Given that the reset process of the qubits remains consistent across multiple runs, it can be inferred

that the dissipated energy of microwave photons resulting from the demon's work is same in each run. The obtained results confirm the linear correlation between non-locality, as demonstrated in EPR steering, and the work done by the demon. The largest value of S_2 is 0.770 ± 0.005 , which exceeds the classical bound of $1/\sqrt{2}$ by 12.6 standard deviations. We conducted quantum state tomography to examine the simulated Bell state of Alice-Bob in the largest S_2 case and obtained average fidelity of 0.951 compared to the ideal Bell state. Due to the imperfection of the current quantum processor [47–49], there exists a deviation between the experimental results and the ideal one described by Eq. (2). The simulation of compiled noisy quantum circuits demonstrates that depolarizing is the primary contributor of noise, as depicted in Fig .3b.

Conclusion. In conclusion, we have experimentally demonstrated the Maxwell demon-assistant EPR steering via the superconducting quantum processor. Our results reveal that quantum correlation can be effectively simulated through the application of work. Furthermore, we have identified the presence of Maxwell demon loophole in the EPR steering. It should be emphasized that in the case of Bell test, the Maxwell demon loophole does not exist, as classical communication between Alice and Bob is prohibited during the task. With current state-of-the-art technologies in superconducting chip [50], we can potentially achieve the Maxwell demon-assistant EPR steering task without the locality loophole. By using the most advanced microwave photon detection technology, it is also possible to realize Maxwell demon loophole-free EPR steering. The Maxwell demon-assistant EPR steering demonstrated provides a novel approach to further explore the interplay between quantum correlation, information theory and thermodynamics.

Acknowledgments: This work is supported by Beijing Academy of Quantum Information Sciences. Yong-Sheng Zhang is supported by National Natural Science Foundation of China (Grant No. 920651131). Heng Fan is supported by Natural Science Foundation of China (Grant No. T2121001). Haifeng Yu acknowledges the support from Natural Science Foundation of China (Grant No. 92365206).

-
- [1] A. Einstein, B. Podolsky, and N. Rosen, Can Quantum-Mechanical Description of Physical Reality Be Considered Complete? *Phys. Rev.* **47**, 777 (1935).
- [2] N. Bohr, Can Quantum-Mechanical Description of Physical Reality Be Considered Complete? *Phys.*

- Rev. **48**, 696 (1935).
- [3] N. Brunner, D. Cavalcanti, S. Pironio, V. Scarani, and S. Wehner, Bell nonlocality, Rev. Mod. Phys. **86**, 419 (2014).
- [4] J. S. Bell, On the Einstein-Podolsky-Rosen Paradox, Physics **1**, 195 (1964).
- [5] J. F. Clauser, M. A. Horne, A. Shimony, and R. A. Holt, Proposed Experiment to Test Local Hidden Variable Theories, Phys. Rev. Lett. **23**, 880 (1969).
- [6] J. F. Clauser and M. A. Horne, Experimental consequences of objective local theories, Phys. Rev. D **10**, 526 (1974)
- [7] A. Aspect, Proposed experiment to test the nonseparability of quantum mechanics, Phys. Rev. D **14**, 1944 (1976).
- [8] A. Aspect, P. Grangier, and G. Roger, Experimental Tests of Realistic Local Theories via Bell's Theorem, Phys. Rev. Lett. **47**, 460 (1981).
- [9] A. Aspect, J. Dalibard, and G. Roger, Experimental Test of Bell's Inequalities Using Time-Varying Analyzers, Phys. Rev. Lett. **49**, 1804 (1982).
- [10] A. Aspect, P. Grangier, and G. Roger, Experimental Realization of Einstein-Podolsky-Rosen-Bohm Gedankenexperiment: A New Violation of Bell's Inequalities, Phys. Rev. Lett. **49**, 91 (1982).
- [11] G. Weihs, T. Jennewein, C. Simon, H. Weinfurter, and A. Zeilinger, Violation of Bell's Inequality under Strict Einstein Locality Conditions, Phys. Rev. Lett. **81**, 5039 (1998).
- [12] B. G. Christensen *et al.*, Detection-Loophole-Free Test of Quantum Nonlocality, and Applications, Phys. Rev. Lett. **111**, 130406 (2013).
- [13] M. Giustina *et al.*, Bell violation using entangled photons without the fair-sampling assumption, Nature **497**, 227 (2013).
- [14] B. Hensen *et al.*, Loophole-free Bell inequality violation using electron spins separated by 1.3 kilometres, Nature **526**, 682 (2015).
- [15] M. Giustina *et al.*, Significant-Loophole-Free Test of Bell's Theorem with Entangled Photons, Phys. Rev. Lett. **115**, 250401 (2015).
- [16] L. K. Shalm *et al.*, Strong Loophole-Free Test of Local Realism, Phys. Rev. Lett. **115**, 250402 (2015).
- [17] H. M. Wiseman, S. J. Jones, and A. C. Doherty, Steering, Entanglement, Nonlocality, and the Einstein-Podolsky-Rosen Paradox, Phys. Rev. Lett. **98**, 140402 (2007).
- [18] S. J. Jones, H. M. Wiseman, and A. C. Doherty, Entanglement, Einstein-Podolsky-Rosen correlations, Bell nonlocality, and steering, Phys. Rev. A **76**, 052116 (2007).

- [19] K. Maruyama, F. Nori, and V. Vedral, Colloquium: The physics of Maxwell's demon and information, *Rev. Mod. Phys.* **81**, 1 (2009).
- [20] J. Maddox, Maxwell's demon: Slamming the door, *Nature*, **417**, 903 (2002).
- [21] W. H. Zurek, Maxwell's Demon, Szilard's Engine and Quantum Measurements, *Frontiers of Nonequilibrium Statistical Physics*, pp151-161, Plenum Press, New York 1986. also see arXiv:quant-ph/0301076.
- [22] W. H. Zurek, Quantum discord and Maxwell's demons, *Phys. Rev. A* **67**, 012320 (2003).
- [23] J. Oppenheim, M. Horodecki, P. Horodecki, and R. Horodecki, Thermodynamical Approach to Quantify Quantum Correlations, *Phys. Rev. Lett.* **89**, 180402 (2002).
- [24] V. Giovannetti, Separability conditions from entropic uncertainty relations, *Phys. Rev. A* **70**, 012102 (2004).
- [25] O. Gühne and M. Lewenstein, Entropic uncertainty relations and entanglement, *Phys. Rev. A* **70**, 022316 (2004).
- [26] B. Groisman, S. Popescu, and A. Winter, Quantum, classical, and total amount of correlations in a quantum state, *Phys. Rev. A* **72**, 022317 (2005).
- [27] K. Maruyama, F. Morikoshi, and V. Vedral, Thermodynamical detection of entanglement by Maxwell's demons, *Phys. Rev. A* **71**, 012108 (2005).
- [28] J. V. Koski, V. F. Maisi, T. Sagawa, and J. P. Pekola, Experimental Observation of the Role of Mutual Information in the Nonequilibrium Dynamics of a Maxwell Demon, *Phys. Rev. Lett.* **113**, 030601 (2014).
- [29] J. V. Kosi, V. F. Maisi, J. P. Pekola, and D. V. Averin, Experimental realization of a Szilard engine with a single electron, *PNAS* **111**, 13786-13789 (2014).
- [30] Y. Zou, Y. Jiang, Y. Mei, X. Guo, and S. Du, Quantum Heat Engine Using Electromagnetically Induced Transparency, *Phys. Rev. Lett.* **119**, 050602 (2017).
- [31] K. Ono, S. N. Shevchenko, T. Mori, S. Moriyama, and F. Nori, Analog of a Quantum Heat Engine Using a Single-Spin Qubit, *Phys. Rev. Lett.* **125**, 166802 (2020).
- [32] Q. Bouton, J. Nettersheim, S. Burgardt, D. Adam, E. Lutz, and A. Widera, A quantum heat engine driven by atomic collisions, *Nat. Commun.* **12** 1-7 (2021).
- [33] T. D. Kieu, The Second Law, Maxwell's Demon, and Work Derivable From Quantum Heat Engines, *Phys. Rev. Lett.* **93**, 140403 (2004).
- [34] K. Beyer, K. Luoma, and W. T. Strunz, Steering heat engines: A truly quantum Maxwell demon, *Phys.*

- Rev. Lett. **123**, 250606 (2019).
- [35] C. Elouard, D. Herrera-Martí, B. Huard, and A. Auffèves, Extracting Work from Quantum Measurement in Maxwell's Demon Engines, Phys. Rev. Lett. **118**, 260603 (2017).
- [36] K. Funo, Y. Watanabe, and M. Ueda, Thermodynamic work gain from entanglement, Phys. Rev. A **88**, 052319 (2013).
- [37] M. Perarnau-Llobet, K. V. Hovhannisyán, M. Huber, P. Skrzypczyk, N. Brunner, and A. Acín, Extractable Work from Correlations, Phys. Rev. X **5**, 041011 (2015).
- [38] M. A. Ciampini, L. Mancino, A. Orioux, C. Vigliar, P. Mataloni, M. Paternostro, and M. Barbieri, Experimental extractable work-based multipartite separability criteria, NPJ Quantum Inf. **3**, 10 (2017).
- [39] M. J. Hu, X. M. Hu, and Y. S. Zhang, Maxwell Demon and Einstein-Podolsky-Rosen Steering, arXiv:2105.05656v2.
- [40] S. Lloyd, Quantum-mechanical Maxwell's demon, Phys. Rev. A **56**, 3374 (1997).
- [41] J. Preskill, Quantum Computing in the NISQ Era and Beyond, Quantum **2**, 79 (2018).
- [42] R. Landauer, Irreversibility and Heat Generation in the Computing Process, IBM J. Res. Dev. **5**, 183 (1961).
- [43] X. G. Li *et al.*, Vacuum-gap transmon qubits realized using flip-chip technology, Appl. Phys. Lett. **119**, 184003 (2021).
- [44] J. M. Gambetta, F. Motzoi, S. T. Merkel, and F. K. Wilhelm, Analytic control methods for high-fidelity unitary operations in a weakly nonlinear oscillator, Phys. Rev. A **83**, 012308 (2011).
- [45] E. Knill, D. Leibfried, R. Reichle, J. Britton, R. B. Blakestad, J. D. Jost, C. Langer, R. Ozeri, S. Seidelin, and D. J. Wineland, Randomized benchmarking of quantum gates, Phys. Rev. A **77**, 012307 (2008).
- [46] S. Boixo, S. V. Isakov, V. N. Smelyanskiy, R. Babbush, N. Ding, Z. Jiang, M. J. Bremner, J. M. Martinis, and H. Neven, Characterizing quantum supremacy in near-term devices, Nat. Phys. **14**, 595 (2018).
- [47] F. Arute *et al.*, Quantum supremacy using a programmable superconducting processor, Nature **574**, 505 (2019).
- [48] Y. L. Wu *et al.*, Strong Quantum Computational Advantage Using a Superconducting Quantum Processor, Phys. Rev. Lett. **127**, 180501 (2021).
- [49] Q. L. Zhu *et al.*, Quantum Computational Advantage via 60-Qubit 24-Cycle Random Circuit Sampling, Sci. Bull. **67**, 240 (2022).

- [50] S. Storz *et al.*, Loophole-free Bell inequality violation with superconducting circuits, *Nature* **617**, 265 (2022).

Appendix A: Device information

As shown in Fig. 4, the superconducting quantum processor consists of 9 qubits and 12 couplers. These components are organized in a two-dimensional square lattice. The superconducting transmon qubit is symbolized by the cross, whereas the rectangular block denotes the coupler. Each qubit within the device is configured in the Xmon architecture, which consists of either two symmetric Josephson junctions or a dc-SQUID. Additionally, each qubit is equipped with a control line that integrates both microwave drive (XY control) and flux bias (Z control). Additionally, each qubit is capacitively coupled to a quarter-wave resonator, which is subsequently linked to a Purcell filter for the purpose of dispersive readout. The 9 qubits are partitioned into 3 groups, where each group consists of 3 qubits that share a transmission line. The coupling between nearest-neighbor qubits, known as qubit-qubit coupling, is influenced by two factors: direct capacitive coupling and indirect coupling through the coupler. Each coupler has an individual flux bias line, allowing for the adjustment of the effective qubit-qubit coupling strength within a range of $\sim +2$ MHz to ~ -50 MHz by manipulating the frequency of the coupler. The implementation of two-qubit CZ gates involves a coupling strength of approximately 9 MHz. The chip is manufactured using the flip-chip technology, incorporating a tantalum base layer.

Four qubits, denoted as q_0 , q_1 , q_2 , and q_4 , were utilized in our experiment (refer to Fig. 4) and the device parameters can be found in Table I. Notably, the frequency of the readout resonator, ω_r , ranges from 7.303 to 7.356 GHz, which is above the maximum qubit frequency ω_{\max} that varies between 4.997 and 5.142 GHz. The idle frequency ω_{idle} is adjusted to be in close proximity to ω_{\max} in order to minimize the impact of flux noise. The energy relaxation time T_1 for each qubit at the idle frequency is found to be greater than $20 \mu\text{s}$. Additionally, the dephasing time T_2^* varies between 1.60 and $4.23 \mu\text{s}$. The fidelity of the single-qubit gate is $\sim 99.9\%$. The coupling strength between the qubit and its connected coupler is ~ 80 MHz, while the direct coupling strength between adjacent qubits is ~ 9 MHz.

In our experiment, all single-qubit gates are performed at the idle frequencies of the qubits. Additional information regarding this can be found in Appendix D. Furthermore, the experimental details of the two-qubit CZ gate are also outlined in Appendix D. The circuits are implemented on the quantum processor using the calibrated single- and two-qubit gates.

Appendix B: Measurement setup

The experiment is performed on a BlueFors XLD dilution refrigerator with a base temperature of 10 mK. In order to enhance the magnetic shielding performance, the refrigerator is equipped with a high-permeability shielding cartridge on its exterior. Additionally, a superconducting sample box containing a superconducting quantum chip is further enclosed within the Cryoperm-10 low-temperature magnetic shielding cartridge.

The experimental setup is depicted in Fig. 4, where we have arranged the different control lines from left to right as follows: Coupler Z control (purple), Qubit control (dark green), Readout control (blue), and Josephson parametric amplifier control (dark red). The Readout control comprises an input line and an output line. The input line is responsible for delivering multi-tone microwave signals to the transmission line, while the output signals undergo amplification through a combination of a Josephson parametric amplifier (JPA), a high electron mobility transistor (HEMT), and a room-temperature microwave amplifier. Finally, the amplified signals undergo demodulation

TABLE I. **Basic parameters of the four qubits, q_0 , q_1 , q_2 , and q_4 , employed in the present experiment. ω_r , ω_{\max} , and ω_{idle} represent the readout resonator frequency, the qubit maximum frequency, and the qubit idle frequency, respectively. α represents the qubit anharmonicity. T_1 and T_2^* represent the energy relaxation time and dephasing time of the qubit at idle point. The readout fidelities for the ground and first-excited states are denoted as F_g and F_e , respectively. The calibration of single-qubit errors is performed using randomized benchmarking (RB).**

Qubit	q_0	q_1	q_2	q_4
$\omega_r/2\pi(\text{GHz})$	7.317	7.303	7.347	7.356
$\omega_{\max}/2\pi(\text{GHz})$	5.142	5.061	4.997	5.097
$\omega_{\text{idle}}/2\pi(\text{GHz})$	5.140	4.908	4.674	4.962
$\alpha/2\pi(\text{MHz})$	-198	-196	-224	-196
$T_1(\mu\text{s})$	39.3	40.8	29.3	24.5
$T_2^*(\mu\text{s})$	4.23	1.60	1.68	3.04
$F_g(\%)$	96.9	95.5	95.3	94.6
$F_e(\%)$	94.0	92.7	92.3	92.7
1Q RB (%)	99.949	99.950	99.902	99.893

through an analog-to-digital converter. To address the constraint of a limited number of control lines on the sample, a Duplexer is employed to merge the qubit XY control line and Z control line prior to their entry into the cryogenic refrigerator. After undergoing a series of attenuators, the combined signals are filtered with a CR124 filter and then combined with the DC line using a bias-Tee. The combined signal is then delivered to the sample at extremely low temperatures. Additionally, the control line for the coupler Z is composed of a flux line and a DC line, which are further integrated at extremely low temperatures using a bias-Tee.

We successfully manipulated a system consisting of four qubits and four couplers by employing 3 microwave sources, 2 ADC channels, 16 DAC channels, and 8 DC sources. Each measurement is conducted over a time period of $310 \mu\text{s}$, which is approximately 10 times the decoherence time of the qubits. This allows enough time for the qubits to reset to their ground states after being operated.

Appendix C: Basic Calibration

After the sample has been cooled, the initial calibration of the sample is conducted using the following steps:

1. Preliminary calibration of the readout frequency.
2. Finding the operating frequency of the JPA to maximize the signal-to-noise ratio of the readout signal.
3. Measuring the functional correlation between the qubit frequency and the voltage bias. Additionally, the avoided crossing spectrum of the qubits and couplers can be measured to estimate the positions of the vertices in the energy spectrum of the coupler. These vertices can then be selected as idle points.
4. Using Rabi measurements to acquire π and $\pi/2$ pulses. By manipulating various parame-

TABLE II. **Basic parameters of two-qubit gates. The fidelities of the two-qubit CZ gate (between q_0 and q_1 , q_1 and q_2 , q_2 and q_4 , and q_1 and q_4) are calibrated by randomized benchmarking (RB).**

Qubit	$q_0 - q_1$	$q_1 - q_2$	$q_2 - q_4$	$q_4 - q_1$
CZ gate length (ns)	53	53	53	53
CZ gate RB (%)	99.53	99.11	98.77	99.26

ters, such as power, envelope, length, and frequencies of the readout pulses, as well as the qubit frequencies during readout, it is possible to enhance the fidelity of the readout process.

5. In order to calibrate the timing of the qubit's XY and Z control lines, we adjust the timing of the $\pi/2$ and Z pulses. Additionally, the timing calibration between qubits and the timing calibration between qubits and couplers is performed through swap experiments involving nearest-neighbor qubits.

6. Measuring the T1 and Ramsey to determine the approximate idle point of the qubit, while taking into account the implementation conditions of the high-fidelity two-qubit gate.

7. By conducting a swap experiment, it is possible to measure the relationship between the coupling strength of adjacent qubits and the coupler bias. Additionally, by setting the turning off frequency of the coupler as the idle point, the coupling strength of the neighboring qubits can be effectively deactivated.

8. To calibrate the distortion of qubits and couplers, conduct a phase change experiment induced by square wave distortion, and then perform the timing calibration again.

Since the XY crosstalk is approximately 3% and the Z crosstalk is below 1%, there is no need to perform XY crosstalk and Z crosstalk calibration in this calibration process.

Appendix D: Calibration of Single-Qubit Gate, Two-Qubit Gate and Readout

In our experiment, the optimized arrangement of idle frequencies is presented in Tab. I. All single-qubit gates are implemented by employing cosine-enveloped pulses at the idle frequency. The pulse length of the $\pm X/2$ and $\pm Y/2$ gates is 20 ns. To mitigate the leakage from the computational space to higher energy levels, the Derivative Removal by Adiabatic Gate (DRAG) technique is utilized. The fidelity of the single-qubit gates, as determined through Randomized Benchmarking at the idle point, is approximately 99.9%.

The two-qubit gate utilized in our experiment is the non-adiabatic CZ gate. To implement the CZ gate, the error function is used as the envelope of the driving pulse function. The energy levels of the qubits are adjusted from their idle frequencies to their working frequencies. At the working frequencies, the energy level of $|101\rangle$ is resonant with $|200\rangle$ ($|002\rangle$), and the coupling between the two qubits is turned on. After accumulating enough phase through resonance, the coupler and qubits return to their idle frequency by employing error function-shaped pulses. The detuning between neighboring qubits at the idle frequency is close to the anharmonicity. Consequently,

the CZ gate can be implemented using a small square pulse, which is advantageous when the calibration of square wave distortion is not perfect. To suppress leakage and achieve the desired conditional phase, we meticulously fine-tune the operating points of the qubits and the coupler. The calibrated CZ gate has a total duration of 53 ns, which includes the rising and falling edges of 6 ns, the phase accumulation time of 39 ns, and a buffer time of 2 ns. Finally, Randomized Benchmarking (RB) is employed to evaluate the performance of the calibrated CZ gates. The resulting fidelities are presented in Tab. II.

Readout calibration begins with the first step of readout classification. The qubits are initialized to the states of $|0\rangle$ and $|1\rangle$, respectively. Subsequently, the readout signals are trained and classified using the python package `sklearn.svm`. The trained classifier is used to calculate the readout fidelity. We quantify the simultaneous readout fidelity of $|0\rangle$ and $|1\rangle$, denoted as F_g and F_e in Tab. I, respectively. Furthermore, to calibrate the readout error in the experimental data, we utilized four readout qubits (q_0, q_1, q_2 , and q_4) into $|ijkl\rangle, i, j, k, l \in \{0, 1\}$ and established a multi-qubit readout matrix.

Appendix E: Compilation and Optimization of Quantum Circuits

The original quantum circuit, consisting of five qubits, was used to implement the experiment (Fig. 2 in the main text). However, it can be divided into three sub-quantum circuits, each containing four qubits (Fig. 5a-c). Figure 5a and b depict the scenario involving the presence of Maxwell’s demon. In the aforementioned quantum circuits, the q_3 in Fig. 2 of the main text is omitted, which acts as a random choice generator for the demon. Instead of q_3 , we employ two sub-quantum circuits to achieve its function. In the circuit of Fig. 5a, q_0 and q_4 are idle during the first time period for the first single qubit gate. However, in the circuit shown in Fig. 5b, two $R_y(-\pi/4)$ gates are applied to qubits q_0 and q_4 . The proportion of circuits a and b is 1:1, and integrating these two circuits can effectively replace the role of qubit q_3 in the initial circuit. Figure 5c represents the scenario in which the demon is absent. In the given circuit, the Control-H gates connecting the demon q_2 to q_0 and q_4 are omitted.

According to the hardware connectivity, we need to compile the circuits shown in Fig. 5a-c into circuits that can be accurately implemented on real hardware. The hardware information is shown in Fig. 4. For circuit compilation, we utilize the CZ gate, a two-qubit gate, along with several single-qubit gates as the elementary gate set to compile all other two-qubit gates. For instance,

the CNOT gate can be compiled into a CZ gate by using two Hadamard gates. There is no direct connection between q_0 and q_2 . To apply the control-H gate between these two qubits, a swap gate is required between q_0 and q_1 in the third layer. Then the compiled circuits for Fig. 5a-c are shown in Fig. 6a-c.

To demonstrate the outcomes when Maxwell's demon performs operations probabilistically, we conducted experiments with five groups. Each group consists of a combination of circuits incorporating Maxwell's demon and circuits without it, with the following ratios: 0:1, 0.2:0.8, 0.4:0.6, 0.8:0.2, and 1:0. Each group includes 200 measurements, and each measurement consists of 2000 shots. The average of the probability values of $P_{\text{target}} = P_{00} + P_{11} - P_{01} - P_{10}$ is calculated for q_0 and q_4 in all circuits. The results are aggregated in proportion to the number of measurements, as depicted in Fig. 3. The error bar represents the mean square deviation of P_{target} calculated from one-tenth of the data, which was obtained by measuring 500 sets of 5 groups randomly. The experimental results provide clear evidence of a linear correlation between the steering parameter S_2 and the operational probability of Maxwell's demon.

In circuits with Maxwell's demon, q_0 and q_4 are theoretically expected to be in the Bell state before the readout process. The measurement results of quantum state tomography are shown in Fig. 7, with fidelities of 96.7% and 93.5%, respectively.

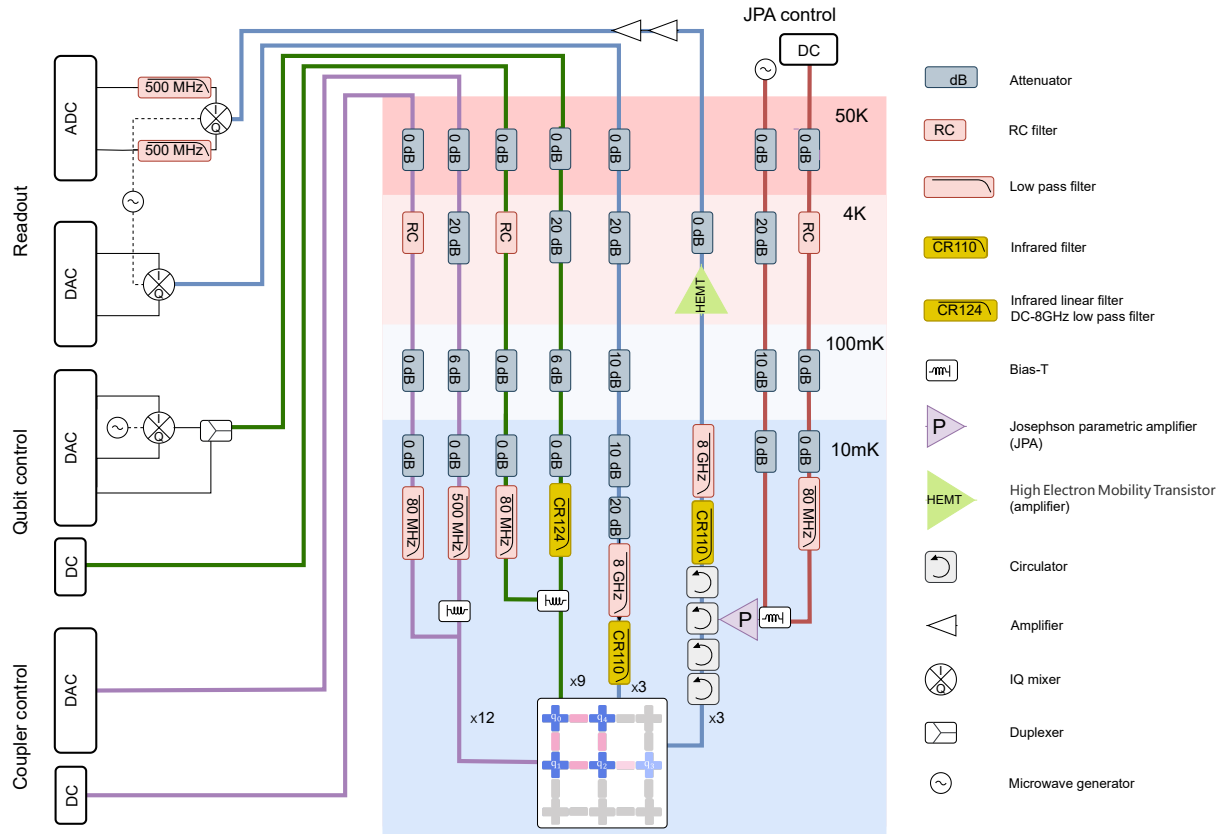


FIG. 4. **Experimental setup.** Electronics and wiring setup illustrating the synthesis and transmission of control/readout signals. Each qubit has three control components: XY (microwave), fast Z (AWG), and slow Z (DC). Each coupler has two control channels: fast Z and slow Z. All control and readout lines are well-attenuated and filtered to provide noise shielding and precise control.

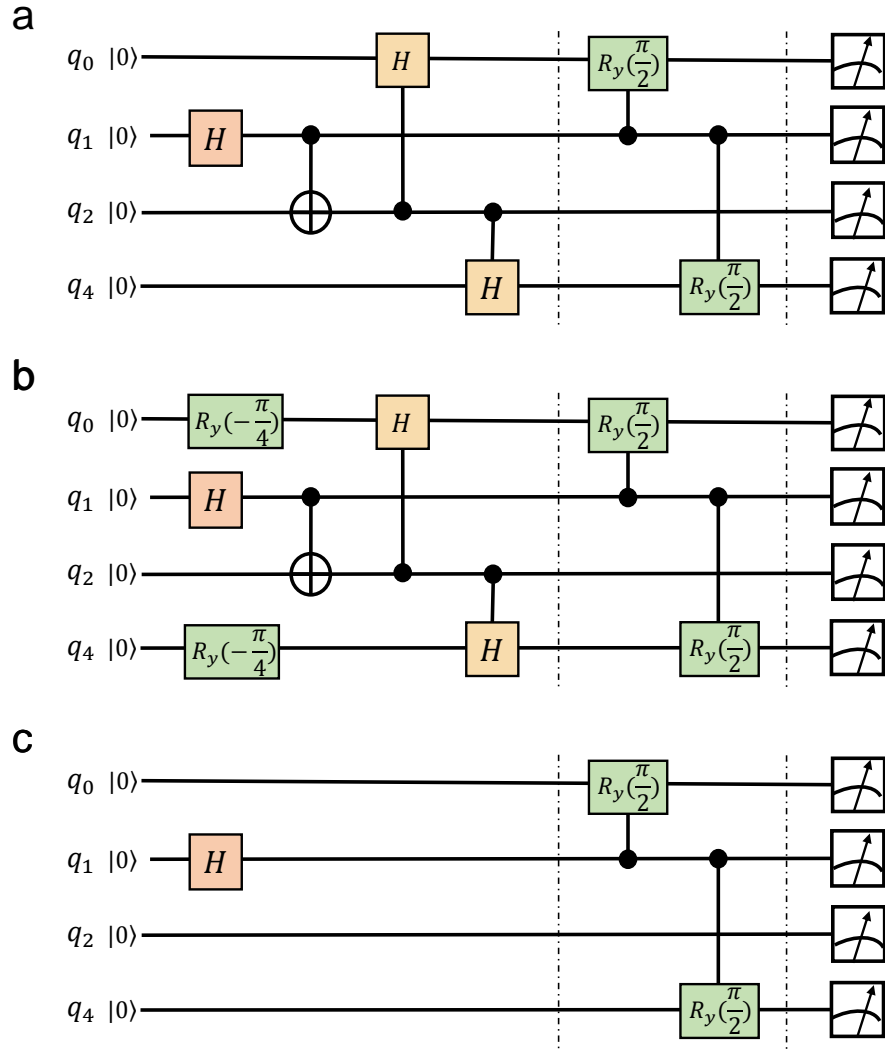


FIG. 5. **Quantum circuit for the experiment.** The original quantum circuit can be split into three sub-quantum circuits. **a** and **b** are for the case where there is the Maxwell demon. **c** is for the case without the Maxwell demon.

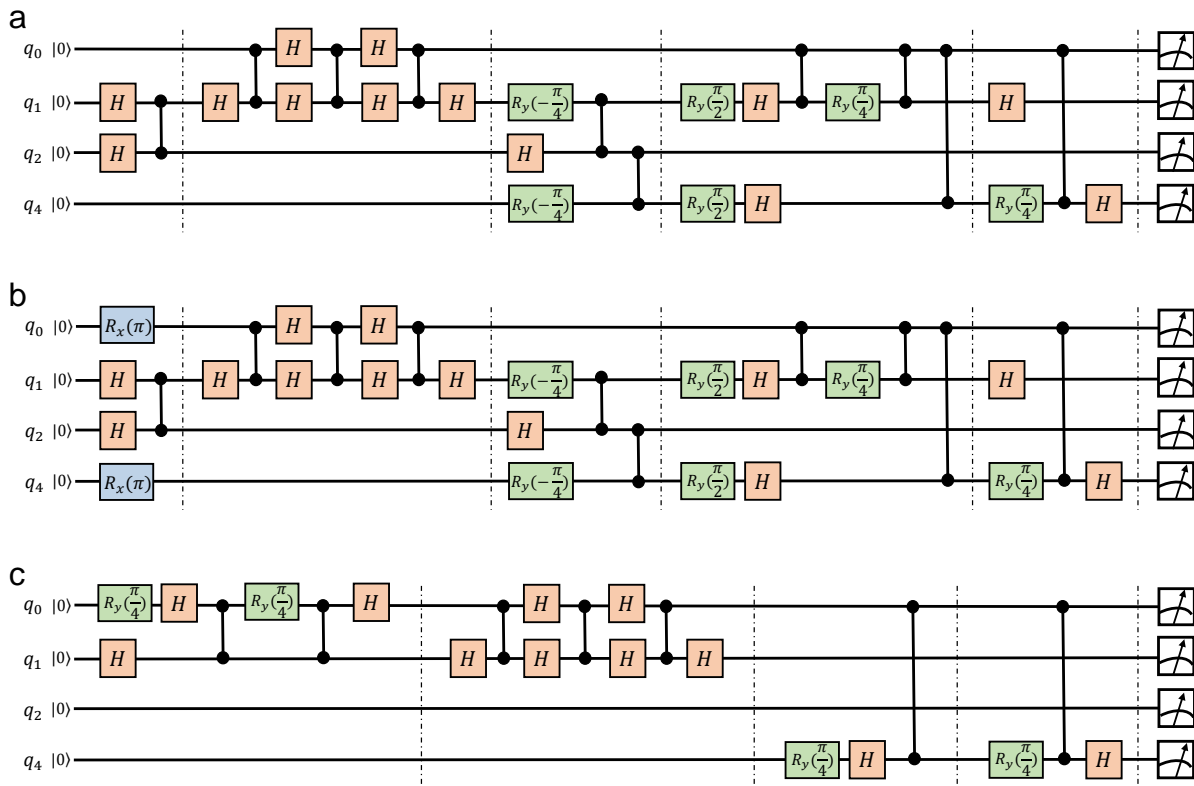


FIG. 6. **Compiled circuits.** According to the hardware connectivity, the circuits in Fig. 5 can be compiled into three new circuits which can be run on our quantum processor.

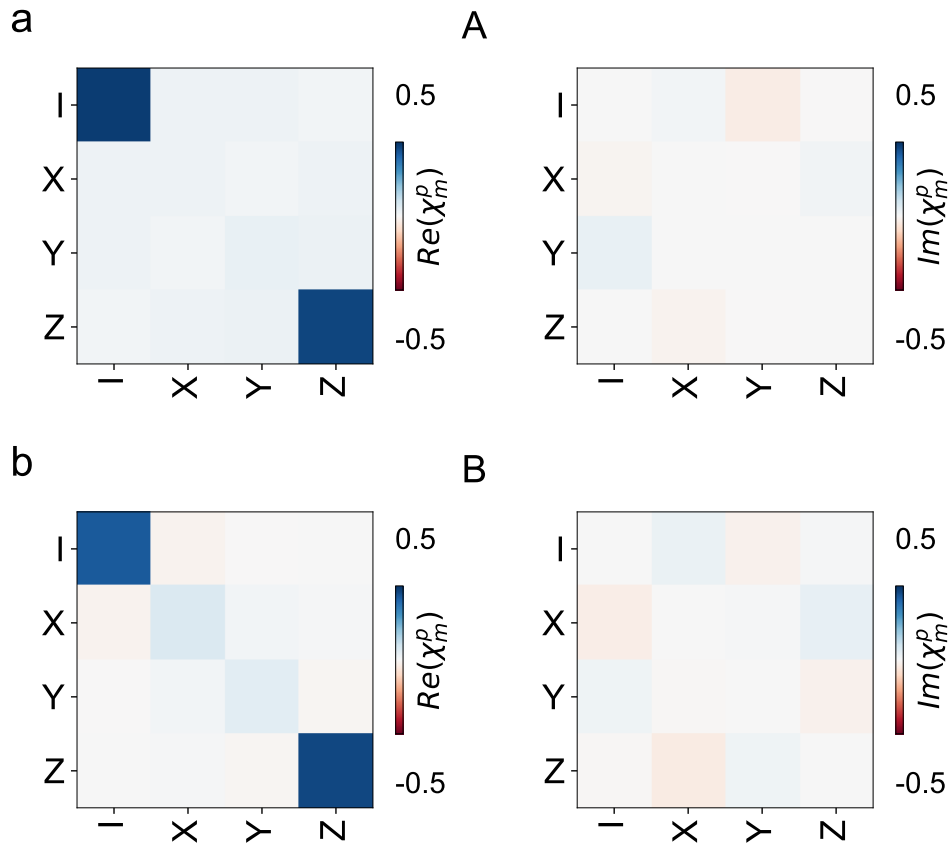


FIG. 7. The measurement results of quantum state tomography for circuits with Maxwell's demon. a: A represents the tomographic measurement result of the circuit shown in Fig. 6a, with a fidelity of 96.7%. **b:** B represents the tomographic measurement result of the circuit shown in Fig. 6b, with a fidelity of 93.5%. Additionally, the left side of the figure corresponds to the real part of the measurement result, while the right side corresponds to the imaginary part.